ACS APPLIED MATERIALS & INTERFACES

Research Article

www.acsami.org

Enhanced Visible Photovoltaic Response of TiO_2 Thin Film with an All-Inorganic Donor–Acceptor Type Polyoxometalate

Jian-Sheng Li,[†] Xiao-Jing Sang,[†] Wei-Lin Chen,*[,†] Lan-Cui Zhang,[‡] Zai-Ming Zhu,[‡] Teng-Ying Ma,[†] Zhong-Min Su,[†] and En-Bo Wang*[,†]

[†]Key Laboratory of Polyoxometalate Science of Ministry of Education, Department of Chemistry, Northeast Normal University, Changchun, Jilin 130024, China

[‡]School of Chemistry and Chemical Engineering, Liaoning Normal University, Dalian 116029, China

Supporting Information

ABSTRACT: In the field of material chemistry, it is of great significance to develop abundant and sustainable materials for solar energy harvesting and management. Herein, after evaluating the energy band characteristics of 13 kinds of polyoxometalates (POMs), the trisubstituted POM compound $K_6H_4[\alpha\text{-}SiW_9O_{37}Co_3(H_2O)_3]\cdot 17H_2O$ (SiW_9Co_3) was first studied due to its relatively smaller band gap (2.23 eV) and higher lowest unoccupied molecular orbital (LUMO) level (−0.63 V vs NHE). Additionally, the preliminary computational modeling indicated that SiW_9Co_3 exhibited the donor–acceptor (D–A) structure, in which the cobalt oxygen clusters and tungsten skeletons act as the electron donor and electron acceptor, respectively. By employing SiW_9Co_3 to modify the TiO_2 film, the visible photovoltaic and photocurrent response were both enhanced, and the light-induced photocurrent at 420 nm was improved by 7.1 times. Moreover, the highly dispersive and small sized SiW_9Co_3 nanoclusters loading on TiO_2 were successfully achieved by fabricating the nanocomposite film of $\{TiO_2/SiW_9Co_3\}_3$ with the layer-by-layer method, which can result in the photovoltaic performance enhancement of dye-sensitized solar cells (DSSCs), of which the overall power conversion efficiency was improved by 25.6% from 6.79% to 8.53% through the synergistic effect of POMs and Ru-complex.

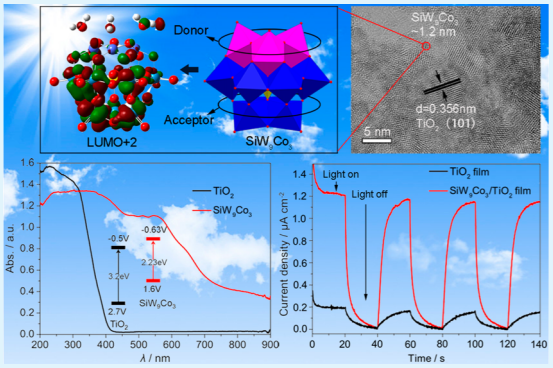

KEYWORDS: *polyoxometalate, photovoltaic, visible, TiO_2, donor–acceptor*

1. INTRODUCTION

Recently, energy and environmental problems have been the two major issues for human society. Solar energy has been the ideal source to satisfy the future energy demand.[1−7] The photovoltaic devices constructed from inorganic semiconductors represent one of the most promising strategies to realize sustainable energy supply.[8−11] TiO_2 nanomaterials appear to be distinguishing candidates owing to its high chemical and optical stability, nontoxicity, and low cost. However, the large band gap (3.2 eV) limits TiO_2 to only exhibit relatively high reactivity under ultraviolet (UV) light, and its photoelectric chemical actions are not activated by visible and infrared light although they were dominant in the solar radiation.[12−15] Great efforts have been devoted to drive TiO_2 toward visible light absorption including certain dye sensitization or doping with metal or nonmetal ions.[16−20]

POMs are a class of unique nanoscale and environmentally friendly transition metal–oxygen clusters composed of earth abundant elements, which exhibit superior optoelectric chemical properties and have enormous potentials on solar energy usage because of their inherent semiconductor-like features.[21−26] POMs have reversible redox properties; their oxidative and reduced state can stably exist simultaneously. Accordingly, POMs are capable of electronic transmission and storage, which represent a valuable and promising building block in the photocatalytic system and photovoltaic devices.[27−31] Besides, their electronic characteristics and energy levels involving the LUMO and the highest occupied molecular orbital (HOMO) can be regulated by adjusting the composition, size, structure, and charge density.[32−35] Furthermore, molecular modification and design laid the foundation for achieving multifunctional POMs because of the high reactivity of surface oxygen sites in POMs. For example, the donor–acceptor structures of POMs have been proposed theoretically, which has been proved to be beneficial for the electronic transmission.[36] Besides, a series of POM-based dye sensitizer based on organoimido-substituted hexamolybdates have been studied and designed via density functional theory.[37] The classical Keggin type POMs have been applied to reduce the exciton recombination in TiO_2.[38,39]

Received: May 6, 2015
Accepted: June 1, 2015
Published: June 1, 2015

DOI: 10.1021/acsami.5b03948
ACS Appl. Mater. Interfaces 2015, 7, 13714−13721

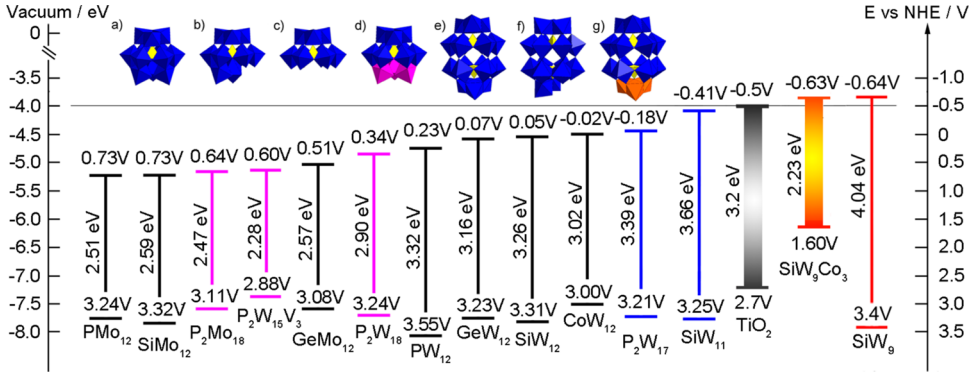

Figure 1. LUMO and HOMO redox potentials vs normal hydrogen electrode (NHE) and energy levels vs vacuum for 14 POMs as well as that of TiO_2. Different colors of lines represented different series of POMs. Their polyhedron structure diagrams were shown in (a) Keggin, (b) monolacunary Keggin, (c) trisubstituted Keggin, (d) Dawson, (e) monolacunary Dawson, and (f) trisubstituted Dawson.

Herein, a series of POMs including Keggin, Dawson, lacunary, and transitional metal trisubstituted structures were investigated systematically to analyze their energy band structures. Thereafter, the trisubstituted SiW_9Co_3 was applied first to modify TiO_2 thin films owing to its smaller band gap and higher LUMO level, which resulted in the final enhanced visible-induced photocurrent and photovoltaic response. Moreover, the nanocomposite film of $\{TiO_2/SiW_9Co_3\}_3$ was assembled with the layer-by-layer method because the depositing layer number of three has been proved to be appropriate for superior photovoltaic performance.[40] The highly dispersed and small sized SiW_9Co_3 nanocluster loading on TiO_2 was successfully achieved, which may result in efficient photovoltaic performance enhancement of DSSCs, and the overall energy conversion efficiency enhanced to 8.53%, that was 25.6% higher than that without modification.

2. EXPERIMENTAL SECTION

2.1. Chemicals and Reagents. All the raw materials employed were used as received without further purifications. The involved POMs are as follows: $H_3PW_{12}O_{40}$ (PW_{12}), $H_4SiW_{12}O_{40}$ (SiW_{12}), $H_4GeW_{12}O_{40}$ (GeW_{12}), $K_6CoW_{12}O_{40}$ (CoW_{12}), $H_3PMo_{12}O_{40}$ (PMo_{12}), $H_3SiMo_{12}O_{40}$ ($SiMo_{12}$), $H_3GeMo_{12}O_{40}$ ($GeMo_{12}$), $H_6P_2Mo_{18}O_{62}$ (P_2Mo_{18}), $K_6P_2W_{18}O_{62}$ (P_2W_{18}), $K_8SiW_{11}O_{39}$ (SiW_{11}), $K_{10}P_2W_{17}O_{61}{\cdot}20H_2O$ (P_2W_{17}), $H_9P_2W_{15}V_3$ ($P_2W_{15}V_3$), SiW_9Co_3, which were prepared according to the literature methods[41−45] and characterized by FTIR (Supporting Information Figure S1), Raman spectra (Supporting Information Figures S2−S4), and TG curves (Supporting Information Figure S5).

2.2. Preparation of SiW_9Co_3-Adsorbed TiO_2 Electrodes. First, the SiW_9Co_3 anion was encapsulated with the cations of dimethyldioctadecyl (DODA) through ion metathesis reactions with a similar reported method,[46] and the product was characterized by FTIR (Supporting Information Figure S6). Second, TiO_2 electrodes were prepared by the screen printing technique.[47] Thereafter, TiO_2 electrode was immersed in the 0.5 mM CH_2Cl_2 solution of DODA-encapsulated SiW_9Co_3 for 4 h to complete the adsorption process. Then the excess SiW_9Co_3 was rinsed off with CH_2Cl_2 and dried with N_2. Finally, a two-electrode system was fabricated to evaluate the photocurrent response under different wavelengths. Specifically, the SiW_9Co_3-adsorbed TiO_2 electrode was covered with a platinum mirror electrode, between which an electrolyte solution composed of 0.1 M LiI, 0.05 M I_2, 0.6 M 1,2-dimethyl-3-propylimidazolium iodide, and 0.5 M 4-*tert*-butylpyridine in 3-methoxypropionitrile was introduced.

2.3. $\{TiO_2/SiW_9Co_3\}_3$ Nanocomposite Film Assembly. The layer-by-layer technique was applied to fabricate the $\{TiO_2/SiW_9Co_3\}_n$ hybrid film. First, TiO_2 colloid was prepared according to a similar reported method.[48] Second, the FTO substrate was ultrasonically treated with the piranha solution to form a hydrophilic surface. Then, the treated glass was alternately dipped into TiO_2 colloid for 5 min and 1.0 mM SiW_9Co_3 solution for 10 min, rinsed with deionized water, and dried in a N_2 stream after each dipping. This process was repeated for three cycles, and the built-up film was expressed as $\{TiO_2/SiW_9Co_3\}_3$.

2.4. Solar Cell Fabrication. The above nanoscale $\{TiO_2/SiW_9Co_3\}_n$ thin film was introduced into DSSCs by screen printing TiO_2 paste on the well-modified FTO to fabricate the photoanode. The contrast experiment was carried out through the similar process except using the pretreated FTO glass by 40 mM $TiCl_4$ at 70 °C for 30 min. Thereafter, the photoanodes were sintered at 400 °C for 30 min and post-treated with 40 mM $TiCl_4$ solution at 70 °C. Then the resulting films were immersed in N719 ethanol solution for 24h. Finally, the sandwich DSSCs were assembled by covering a platinum mirror on the photoanode and introducing electrolyte solution composing of 0.1 M LiI, 0.05 M I_2, 0.6 M 1,2-dimethyl-3-propylimidazolium iodide and 0.5 M 4-*tert*-butylpyridine in 3-methoxypropionitrile by the capillary action.

2.5. Characterization Methods. Cyclic voltammograms were recorded on a CHI601D Electrochemical Workstation (Shanghai Chenhua Instrument Corp., China), using glassy carbon electrode as the working electrode, a Pt wire as the counter electrode, and Ag/AgCl reference electrode. The solid diffuse reflectivity spectra was collected on SHIMADZU UV−vis spectrophotometer UV-2600, which was measured from 200 to 800 nm using $BaSO_4$ as a standard with 100% reflectance. The surface photovoltage spectroscopy measurement was carried out on a lab-made instrument, which constitutes a source of monochromatic light, a lock-in amplifier (SR830-DSP) with a light chopper (SR540), and a photovoltaic cell. A 500 W xenon lamp (CHFXQ500 W, Global xenon lamp power) and a double-prism monochromator (Hilger and Watts, D300) provide monochromatic light. The construction of the photovoltaic cell was a sandwich-like structure of ITO−sample−ITO. AFM images were taken on a silicon slide by a Digital Instruments Nanoscope IIIa instrument operating in contact mode with silicon nitride tips. XPS was performed on F-doped SnO_2 glass using an ESCALAB-MK$\prod$ photoelectronic spectrometer with a Mg Kα (1253.6 eV) achromatic X-ray source. The nanostructures were characterized with high resolution transmission electron microscope (HRTEM) (JEOL-2100F) at an acceleration voltage of 200 kV.

3. RESULTS AND DISCUSSION

3.1. Photoelectrochemical Characterization of POMs. In order to preliminarily recognize the electronic characteristics of different POM building blocks, 13 kinds of POMs were purposefully investigated to evaluate their energy band structures, including the classical Keggin and Dawson POMs, the lacunary as well as the transitional metal trisubstituted structures, with the solid diffuse reflection method (Supporting Information Figures S7−S8) and the cyclic voltammetry

DOI: 10.1021/acsami.5b03948
ACS Appl. Mater. Interfaces 2015, 7, 13714−13721

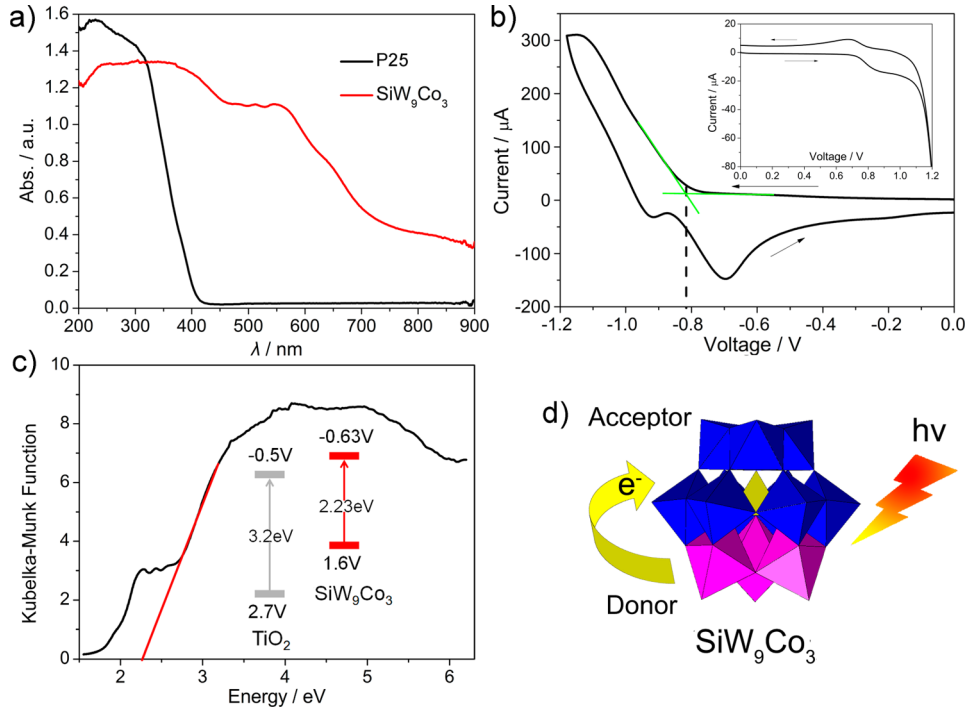

Figure 2. (a) UV−vis diffuse reflectance spectra of P25 (dark line) and SiW_9Co_3 (red line). (b) Cyclic voltammograms of SiW_9Co_3 in LiAc/HAc buffer solution at pH = 6.0. The onset reduction potential was determined as the intersection of the *x* axis and dashed line that was determined by finding out the intersection point between two tangents from the linear portion of the first reduction peak and baseline. (c) The plot of *F* against energy *E* for SiW_9Co_3 and the inset are the schematic energy levels of TiO_2 and SiW_9Co_3. (d) The schematic charge-transfer process in D−A type SiW_9Co_3: Co, purple polyhedron; W, blue polyhedron.

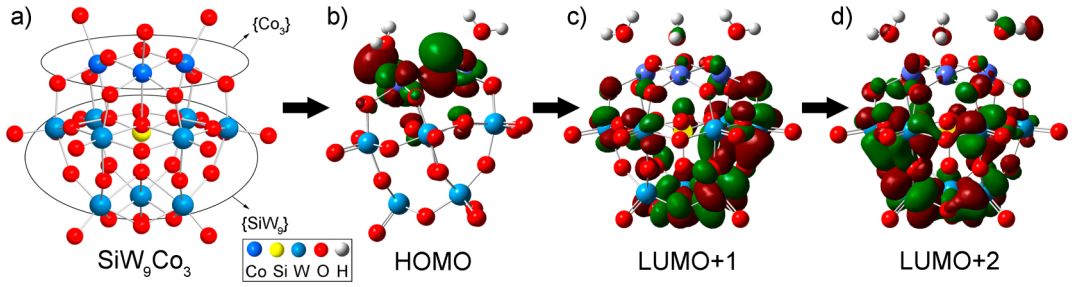

Figure 3. Several simulated molecular orbitals of SiW_9Co_3. Color code: Co, deep blue; W, light blue; O, red.

(Supporting Information Figure S9). Their energy band structures, namely, the HOMO and LUMO positions have been systematically classified and compared with that of TiO_2 in Figure 1. Their relationship was summarized as follows: The band gap of POMs can be tailored by changing their structures and composition. POMs based on W series usually featured larger E_g than Mo series. Saturation reduction of POMs can induce the increase of band gap that can also be adjusted by introducing transitional metals. Meanwhile, the LUMO energy levels of POMs are associated with the central atom and coordinated atoms. A smaller oxidation number of central atom resulted in a higher LUMO level when POMs have the same structures and coordinated atoms. For instance, the LUMO levels of POMs follow the following order: CoW_{12} > SiW_{12} (GeW_{12}) > PW_{12}. Additionally, POMs based on W series showed higher LUMO than Mo series when their structures and central atoms are the same. Further, we can see most POMs featured larger band gaps and lower LUMO as compared with those of TiO_2. In contrast, by incorporating three Co^{2+} ions to the SiW_9 subunit, SiW_9Co_3 featured a relatively narrower band gap (2.23 eV) and higher LUMO level (−0.63 V vs NHE). It is known that a more narrow band gap normally results in stronger visible response, and the higher LUMO can be advantageous to the electronic injection into TiO_2. Thereby, of all the involved POMs, SiW_9Co_3 was most expected to act as the modifier for driving TiO_2 toward visible utilization.

Figure 2a compared the absorption spectra of P25 and SiW_9Co_3 powder, which illustrated that SiW_9Co_3 exhibited the broad optical absorption covering throughout the whole of UV and visible regions whereas P25 absorbed only UV light below 400 nm. In addition, the optical band gap (E_g) of SiW_9Co_3 could be estimated by its diffuse reflection spectrum, from which a plot of *K-M* function *F* against energy *E* was drawn (Figure 2c) and E_g was determined as the intersection point between the energy axis and the line extrapolated from the linear portion of the absorption edge in the plot.[49] Finally, the estimated E_g of SiW_9Co_3 (2.23 eV) demonstrated it exhibited the semiconductor-like feature.

DOI: 10.1021/acsami.5b03948
ACS Appl. Mater. Interfaces 2015, 7, 13714−13721

The redox property of SiW_9Co_3 was evaluated by the cyclic voltammetry in the deoxygenated LiAc/HAc electrolyte solution with pH value of 6.0 using a three-electrode system comprising a glassy carbon working electrode, a platinum wire counter electrode, and Ag/AgCl reference electrode. As shown in the inset of Figure 2b, the redox peaks between 0.6 and 0.9 V were assigned to the oxidation and reduction processes of the $\{Co_3\}$ moiety, and the reduction and reoxidation peaks of the tungsten framework were located in the voltage region from −0.6 to −1.2 V. The cathodic peak at −1.1 V corresponded to two anodic peaks at −0.93 and −0.7 V, respectively, indicating that the reduction of tungsten was related to a multielectron process and their reoxidation was stepwise. Because the LUMO of POMs is the combination of d orbitals centered on the tungsten atoms,[50] the LUMO energy levels could be estimated by finding out the applied potential for the first reduction. Furthermore, because the reduction of SiW_9Co_3 involved a multielectron process, the onset reduction potential (−0.63 V vs NHE) of SiW_9Co_3 presented the average position of its LUMOs. Conclusively, the energy level scheme of TiO_2 and SiW_9Co_3 was shown in the inset of Figure 2b.

Furthermore, the molecular orbital of SiW_9Co_3 was preliminarily studied by the computational modeling (Figure 3),[51] which illustrated that the HOMO and LUMO of SiW_9Co_3 were located on the cobalt oxygen clusters and tungsten framework, respectively, indicating that optical irradiation would induce electronic transmission from the $\{Co_3\}$ unit to the $\{W_9\}$ framework. Accordingly, SiW_9Co_3 could be regarded as a kind of donor−acceptor type POM, and the cobalt oxygen clusters and tungsten framework act as the electron donor and electron acceptor, respectively. Figure 2d illustrated the electronic transmission process scheme from the electron donor to the electron acceptor of SiW_9Co_3 upon light excitation. The surface photovoltage spectrum (SPV) was conducted to characterize the charge transfer at the interface of P25 particles and SiW_9Co_3 upon optical excitation.[52] From Supporting Information Figure S10 we can see that P25 exhibited a sole photovoltage peak around 360 nm, which was ascribed to the charge separation upon only UV light excitation because of the large band gap of TiO_2. Nevertheless, the SPV response of P25/SiW_9Co_3 composite displayed two characteristic peaks, which were possibly attributed to the photogenerated charge transfer between SiW_9Co_3 and P25 particles. Notably, in the visible region, P25/SiW_9Co_3 composite exhibited higher photovoltage than bare P25, which demonstrated that modification of SiW_9Co_3 could broaden the optical response range of TiO_2.

3.2. SiW_9Co_3-Adsorbed TiO_2 Photoanode. The as-prepared P25 electrode by screen printing was adsorbed by SiW_9Co_3 by soaking the photoanode in the CH_2Cl_2 solution of DODA encapsulated SiW_9Co_3. Its adsorption on titanium electrode was mainly derived from the interaction between the hydroxyl groups carried on TiO_2 nanoparticles[53] and the surface oxygen active site of POMs. The adsorbed amount of POMs was semiquantitatively analyzed by EDS (Supporting Information Figure S11). It can be concluded that the mass fraction of SiW_9Co_3 in TiO_2 electrode was 18% based on W and Ti. XPS spectrum and AFM images were recorded to characterize the composite film. The XPS spectrum (Figure 4a,b) was applied to detect the oxidation states of W and Co elements in the composite film, which also confirmed the successful immobilization of SiW_9Co_3 on the surface of P25 film. The XPS spectrum for W_{4f} exhibited two peaks at ca. 35.3

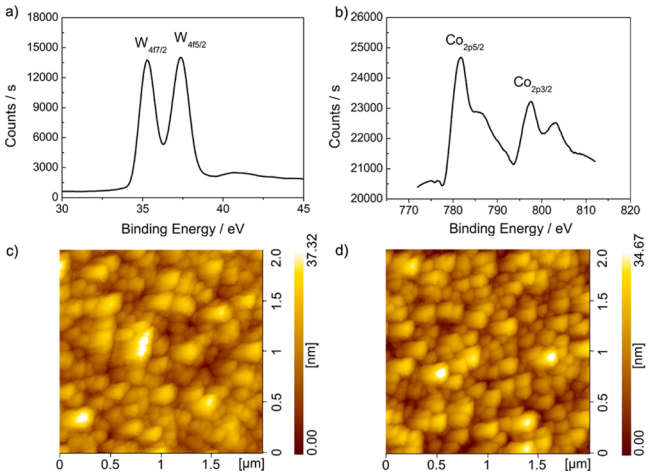

Figure 4. XPS spectrum of SiW_9Co_3-adsorbed P25 film for (a) W_{4f} and (b) Co_{2p}. AFM images in the tapping mode of (c) P25 film and (d) SiW_9Co_3-adsorbed P25 film.

and 37.4 eV, corresponding to the binding energy of $W_{4f7/2}$ and $W_{4f5/2}$, which were consistent with the oxidation state of W^{VI}.[54] The XPS spectrum for Co_{2p} showed two peaks at ca. 781.7 eV in the energy region of $Co_{2p3/2}$ and 797.6 eV in the energy region of $Co_{2p1/2}$, which were consistent with the oxidation state of Co^{II}.[55] These results were consistent with those of isolated SiW_9Co_3 powder (Supporting Information Figure S12), which demonstrated that SiW_9Co_3 was stable during its incorporation in TiO_2 film. The surface morphology and homogeneity of P25 film and SiW_9Co_3-adsorbed P25 film were presented by AFM images. Compared with a P25 film (Figure 4c) that had an average surface roughness R_a of 4.725 nm, the surface of SiW_9Co_3-adsorbed P25 film (Figure 4d) became rougher with R_a of 5.155 nm, and was covered by more tiny granules, which was assigned to the penetration of SiW_9Co_3 among TiO_2 nanoparticles. Besides, no large agglomeration appeared, indicating the uniform distribution of SiW_9Co_3.

A two-electrode system cell was fabricated to evaluate the photocurrent response of P25 film in the presence and absence of SiW_9Co_3, respectively. Figure 5 showed the photocurrent−time curves of two kinds of electrodes under different monochromatic illumination. As was concluded, SiW_9Co_3-adsorbed P25 film had significantly higher anodic photocurrent than bare P25 electrode upon irradiation from 400 to 450 nm,

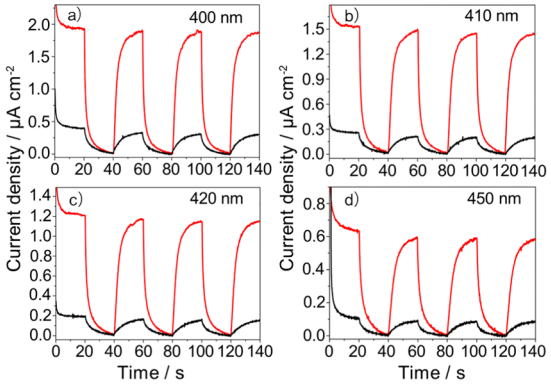

Figure 5. Photocurrent density−time curves of SiW_9Co_3-adsorbed P25 film (red line) and bare P25 film (dark line) under light irradiation at (a) 400, (b) 410, (c) 420, and (d) 450 nm.

DOI: 10.1021/acsami.5b03948
ACS Appl. Mater. Interfaces 2015, 7, 13714−13721

and especially the 420 nm light-induced photocurrent was increased by 7.1 times, which probably resulted from the generated photocurrent by the modification of SiW_9Co_3 upon excitation of visible light. This result was consistent with that of the SPV results, demonstrating that SiW_9Co_3 could expand the photoresponce of TiO_2 from UV to visible light region. To further compare the effect of SiW_9Co_3, the photocurrent response curves of SiW_{12}-, SiW_{11}-, and SiW_9-adsorbed P25 films upon irradiation from 400 to 420 nm were also recorded (Supporting Information Figure S13), which illustrated that SiW_9Co_3 displayed the highest photocurrent whereas SiW_{12}, SiW_{11}, and SiW_9 did not exhibit the positive effect. This maybe resulted from either their larger band gaps or lower LUMO levels, which further indicated that the superior optoelectronic performance of SiW_9Co_3 contributed to the visible photovoltaic response. The insufficient photovoltaic response of SiW_9 may be attributed to its large band gap despite its higher LUMO. Additionally, the current−voltage characteristics of the two-electrode cell constructed from the SiW_9Co_3-absorbed TiO_2 film under the simulated AM 1.5 irradiation were evaluated (Supporting Information Figure S14), and the photovoltaic parameters were listed in Supporting Information Table S2. A short-circuit current density (J_{sc}) of 1.2 mA cm^{-2} and an open-circuit voltage (V_{oc}) of 0.423 V were produced with a fill factor (FF) of 0.597, giving a power conversion efficiency of 0.3%, whereas a bare TiO_2 film gave an efficiency of 0.1% (data not shown), which further confirmed the positive photovoltaic effect of SiW_9Co_3. The dark current density measurement in Supporting Information Figure S15 indicated that SiW_9Co_3-based solar cell had lower dark current density than bare TiO_2 solar cell, which demonstrated that the modification of SiW_9Co_3 successfully retarded the dark current. This was possibly ascribed to the coverage of SiW_9Co_3 on TiO_2 that hindered the contact of conduction band electrons with electrolyte.

3.3. $\{TiO_2/SiW_9Co_3\}_3$ Nanocomposite Film. In order to probe the synergistic effect of SiW_9Co_3 in the DSSCs, a SiW_9Co_3-modified TiO_2 nanocomposite film was introduced into the Ru-complex-based photovoltaic cells. Specifically, the layer-by-layer method was applied to assemble the nanoscale $\{TiO_2/SiW_9Co_3\}_3$ composite film, on which the P25 film was subsequently deposited via screen printing. After calcination, N719 adsorption was achieved for the final construction of DSSCs.

UV−vis absorption spectrum was conducted to monitor the growth process of the layer-by-layer film on a quartz substrate. The characteristic absorption peak at ca. 245 nm in Supporting Information Figure S16 was ascribed to SiW_9Co_3, and the increase in the absorbance of SiW_9Co_3 with increasing number of layers indicated the successful incorporation of SiW_9Co_3. The deposition amount ratio of POMs and TiO_2 was semiquantitatively analyzed by EDS (Supporting Information Figures S17−S18), from which the mass fraction of SiW_9Co_3 was evaluated to be 31%. The morphology of TiO_2 nanocrystalline films was characterized by HRTEM. As shown in Figure 6, the lattice spacing of TiO_2 was measured to be 0.345 and 0.356 nm in TiO_2 nanocrystalline film and $\{TiO_2/SiW_9Co_3\}_3$ nanocomposite film, respectively, which can be both assigned to the (101) lattice facet for anatase.[56] Supporting Information Figure S19 revealed that the size of TiO_2 nanocrystalline was about 8 nm. After formation of a composite with SiW_9Co_3, many tiny dark granules dispersed on the surface of TiO_2 nanocrystalline (shown in the red circle of Figure 6b), and the size of granules was about 1.2 nm, which was just consistent with the size of Keggin anion. The absent lattice fringe of POMs indicated that SiW_9Co_3 existed in the form of dispersed and individual clusters on the surface of TiO_2 and not in the crystalline state.[57,58] Electrostatic attraction between TiO_2 and POMs exists because the TiO_2 surface is positively charged in acidic conditions[59] whereas POMs carry negative charge. Interaction between them can benefit the high dispersion and small size of POM clusters, resulting in avoided aggregation and more accessible surface active sites, which was expected to facilitate the electron transfer between POMs and TiO_2 and be beneficial to the photovoltaic response.

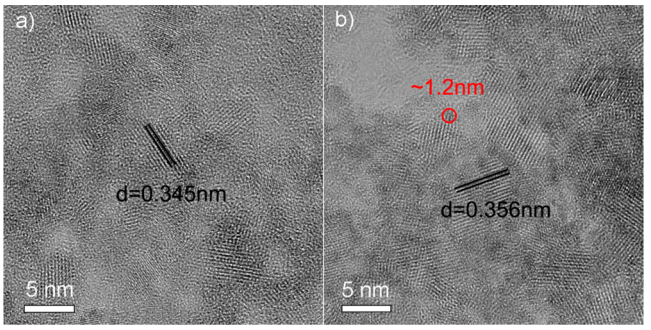

Figure 6. HRTEM images of (a) TiO_2 nanocrystalline film and (b) $\{TiO_2/SiW_9Co_3\}_3$ nanocomposite film.

The cross-sectional SEM image of the final fabricated photoanode is shown in Figure 7, which illustrated that $\{TiO_2/SiW_9Co_3\}_3$ nanocomposite film was deposited between the FTO substrate and P25 layer, and it displayed a more dense structure than the P25 layer, which was due to the smaller size of nanocrystalline TiO_2.

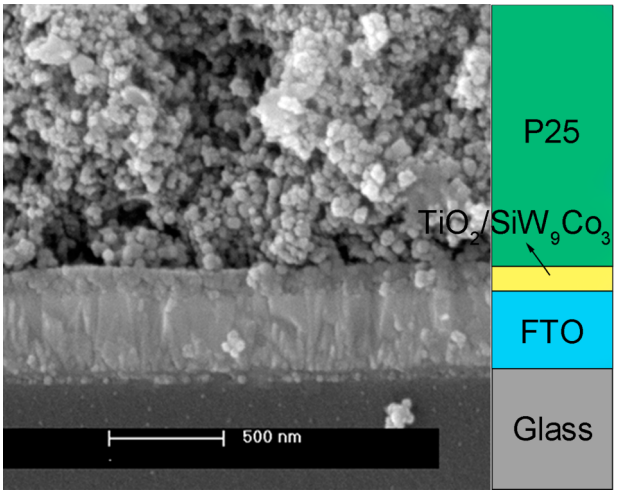

Figure 7. Cross-sectional SEM image of the photoanode film consisting of $\{TiO_2/SiW_9Co_3\}_3$ nanocomposite film and P25 film.

3.4. DSSCs Performance. The performance of DSSCs with a $\{TiO_2/SiW_9Co_3\}_3$ nanocomposite film (cell 1) was evaluated under simulated AM 1.5 illumination (100 mW cm^{-2}) (Figure 8a). The detailed photovoltaic parameters were summarized in Supporting Information Table S3. To assess the reproducibility of DSSCs, three sets of parallel experiments were carried out for each DSSC. The photocurrent−voltage (J−V) results showed that the photovoltaic performance of cell 1 was enhanced compared with that of DSSCs with no treatment of

DOI: 10.1021/acsami.5b03948
ACS Appl. Mater. Interfaces 2015, 7, 13714−13721

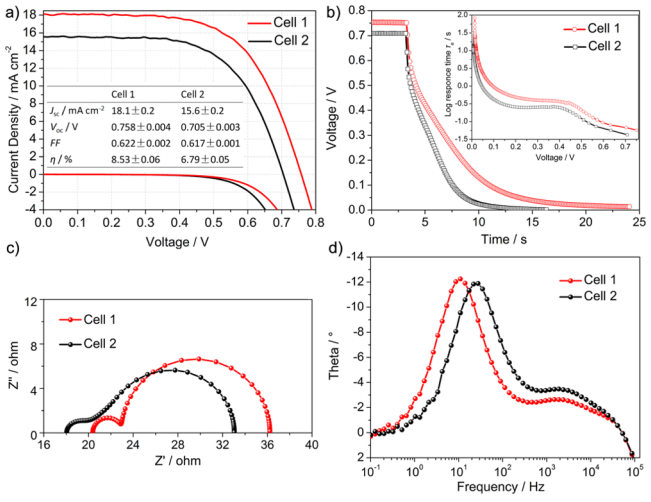

Figure 8. (a) Current density−voltage characteristic of DSSCs with (cell 1) and without (cell 2) $\{TiO_2/SiW_9Co_3\}_3$ nanocomposite film under the simulated AM 1.5 solar illumination of 100 mW cm^{-2} and under dark conditions, respectively. (b) The OCVD curves of cell 1 and cell 2, and the inset is the electron lifetime. The EIS spectra of two kinds of cells: (c) Nyquist plots and (d) Bode phase plots under the simulated AM 1.5 solar illumination of 100 mW cm^{-2} at a forward bias of the open circuit voltage with an ac potential amplitude of 10 mV and a frequency range from 1 Hz to 100 kHz.

SiW_9Co_3 (cell 2). By incorporating the $\{TiO_2/SiW_9Co_3\}_3$ nanocomposite film, the J_{sc} was increased from 15.6 to 18.1 mA cm^{-2}. The increase of J_{sc} relates to more efficient electronic injection, transfer, and collection. Because the LUMO of SiW_9Co_3 (−0.63 V vs NHE) mediated the conduction band of TiO_2 (−0.5 V vs NHE) and the excited state of N719 (−0.98 V vs NHE), SiW_9Co_3 tended to facilitate the charge transfer from Ru-complex to TiO_2 and to enhance the electronic injection ability. Additionally, SiW_9Co_3 can synchronously broaden the visible absorption region and improve the visible photocurrent response owing to its smaller band gap. The improvement of V_{oc} from 705 to 758 mV could be ascribed to the reduced carrier recombination that occurred at the interface of FTO/electrolyte and TiO_2/dye/electrolyte. Finally, the overall photoelectric conversion efficiency was improved by 25.6% from 6.79% to 8.53%.

The open-circuit voltage decay (OCVD) curve monitors the decay process of V_{oc} after turning off the illumination.[60] As shown in Figure 8b, the V_{oc} decayed more slowly for cell 1 than for cell 2, which means the carrier recombination rate in cell 1 was lower than that of cell 2. The inset of Figure 8b showed the electron lifetime calculated from the equation $\tau = (kT/e)/(dV/dt)^{-1}$, which illustrated that cell 1 had the longer electron lifetime. On the basis of these results, one can conclude that the electron transmission of the DSSCs was more efficient with the nanocomposite film of $\{TiO_2/SiW_9Co_3\}_3$.

To further study the electron transmission process, electrochemical impedance spectroscopy (EIS) was carried out to reveal the internal resistances in DSSCs. The two semicircles from high to low frequency in the Nyquist curve are classically assigned to the charge-transfer resistance at the interface of the counter electrode and electrolyte (R_{pt}) and the charge-transfer resistance at the TiO_2/dye/electrolyte interface (R_{ct}).[61] As shown in Figure 8c, R_{ct} of cell 1 was larger than that of cell 2, demonstrating an improvement on the retardation of carrier recombination. Furthermore, the electron lifetime can be estimated from the characteristic frequency of the middle semicircle in the Bode plot according to the relation $\tau_e = (2\pi f_{max})^{-1}$, from which the smaller frequency of cell 1 in Figure 8d corresponded to longer electron lifetime, further confirming the result of OCVD analysis.

CONCLUSION

In summary, the donor−acceptor type POM compound has been first applied to modify TiO_2 thin film owing to its earth abundant source, semiconductor-like feature, small optical band gap, and higher LUMO on the basis of energy level regulation of a series of POMs. By modification of the TiO_2 film with SiW_9Co_3, the visible light-induced photocurrent was 7.1 times higher than that of bare TiO_2 film at 420 nm, and the surface photovoltage response of TiO_2 expanded to the visible region. Additionally, the highly dispersed and small sized SiW_9Co_3 nanoclusters were successfully distributed on TiO_2 through fabricating the $\{TiO_2/SiW_9Co_3\}_3$ nanocomposite film with the layer-by-layer method, which can effectively improve the performance of DSSCs after being introduced into the photoanodes. This work opens new opportunities to develop abundant and sustainable materials for solar energy harvesting and management, and also provides guidance for the photoelectrical functionalization of POMs, and opens a new way for driving TiO_2 film toward visible light utilization. Future work will focus on fabricating POM nanomaterials to exploit their application in the fields of energy and materials.

ASSOCIATED CONTENT

Supporting Information

FTIR, Raman spectra, TG curves, solid diffuse reflection spectrum, cyclic voltammograms of the involved 13 POMs and their energy level diagrams; SPV spectroscopy for P25/SiW_9Co_3 composite and P25; the photocurrent density−time curves of SiW_{12}, SiW_{11}-, SiW_9-, and SiW_9Co_3-adsorbed TiO_2 electrodes; the current−voltage characteristic of SiW_9Co_3 constituted two-electrode system cell and dark current density measurement; UV−vis absorption spectra of multilayer films $\{TiO_2/SiW_9Co_3\}_n$; TEM image, EDS analysis of TiO_2 nanocrystalline film and $\{TiO_2/SiW_9Co_3\}_3$ composite film; electrochemical measurement conditions of POMs; and the detailed photovoltaic parameters of DSSCs. The Supporting Information is available free of charge on the ACS Publications website at DOI: 10.1021/acsami.5b03948.

AUTHOR INFORMATION

Corresponding Authors

*E-mail: chenwl@nenu.edu.cn.
*E-mail: wangeb889@nenu.edu.cn.

Author Contributions

The manuscript was written through contributions of all authors. All authors have given approval to the final version of the manuscript. J.-S.L. and X.-J.S. contributed equally.

Notes

The authors declare no competing financial interest.

ACKNOWLEDGMENTS

This work was financially supported by the National Natural Science Foundation of China (No. 21131001 and 21201031), Science and Technology Development Project Foundation of Jilin Province (No. 201201072), Ph. D station Specialized Research Foundation of Ministry of Education for Universities

DOI: 10.1021/acsami.5b03948
ACS Appl. Mater. Interfaces 2015, 7, 13714−13721

(No. 20120043120007), the State Key Laboratory of Luminescence and Applications and the Analysis and Testing Foundation of Northeast Normal University.

REFERENCES

(1) Liu, J.; Liu, Y.; Liu, N.; Han, Y.; Zhang, X.; Huang, H.; Lifshitz, Y.; Lee, S.-T.; Zhong, J.; Kang, Z. Metal-Free Efficient Photocatalyst for Stable Visible Water Splitting via a Two-Electron Pathway. *Science* **2015**, *347* (6225), 970−974.

(2) Busche, C.; Vila-Nadal, L.; Yan, J.; Miras, H. N.; Long, D.-L.; Georgiev, V. P.; Asenov, A.; Pedersen, R. H.; Gadegaard, N.; Mirza, M. M.; Paul, D. J.; Poblet, J. M.; Cronin, L. Design and Fabrication of Memory Devices Based on Nanoscale Polyoxometalate Clusters. *Nature* **2014**, *515* (7528), 545−549.

(3) Yella, A.; Lee, H.-W.; Tsao, H. N.; Yi, C.; Chandiran, A. K.; Nazeeruddin, M. K.; Diau, E. W.-G.; Yeh, C.-Y.; Zakeeruddin, S. M.; Grätzel, M. Porphyrin-Sensitized Solar Cells with Cobalt (II/III)−Based Redox Electrolyte Exceed 12% Efficiency. *Science* **2011**, *334* (6056), 629−634.

(4) Bai, Y.; Zhang, J.; Zhou, D.; Wang, Y.; Zhang, M.; Wang, P. Engineering Organic Sensitizers for Iodine-Free Dye-Sensitized Solar Cells: Red-Shifted Current Response Concomitant with Attenuated Charge Recombination. *J. Am. Chem. Soc.* **2011**, *133* (30), 11442−11445.

(5) Li, B.; Wang, H.; Zhang, B. W.; Hu, P. F.; Chen, C.; Guo, L. Facile Synthesis of One Dimensional AgBr@Ag Nanostructures and Their Visible Light Photocatalytic Properties. *ACS Appl. Mater. Interfaces* **2013**, *5* (23), 12283−12287.

(6) Zhu, W.; Wu, Y.; Wang, S.; Li, W.; Li, X.; Chen, J.; Wang, Z.-s.; Tian, H. Organic D-A-π-A Solar Cell Sensitizers with Improved Stability and Spectral Response. *Adv. Funct. Mater.* **2011**, *21* (4), 756−763.

(7) Liu, B.; Wei, L.; Li, N. N.; Wu, W. P.; Miao, H.; Wang, Y. Y.; Shi, Q. Z. Solvent/Temperature and Dipyridyl Ligands Induced Diverse Coordination Polymers Based on 3-(2′,5′-Dicarboxylphenyl)pyridine. *Cryst. Growth Des.* **2014**, *14* (3), 1110−1127.

(8) Ji, Z.; He, M.; Huang, Z.; Ozkan, U.; Wu, Y. Photostable p-Type Dye-Sensitized Photoelectrochemical Cells for Water Reduction. *J. Am. Chem. Soc.* **2013**, *135* (32), 11696−11699.

(9) Xie, M.; Fu, X.; Jing, L.; Luan, P.; Feng, Y.; Fu, H. Long-Lived, Visible-Light-Excited Charge Carriers of TiO_2/$BiVO_4$ Nanocomposites and their Unexpected Photoactivity for Water Splitting. *Adv. Energy Mater.* **2014**, *4* (5), 1300995.

(10) Zhang, Z.-M.; Zhang, T.; Wang, C.; Lin, Z.; Long, L.-S.; Lin, W. Photosensitizing Metal−Organic Framework Enabling Visible-Light-Driven Proton Reduction by a Wells−Dawson-Type Polyoxometalate. *J. Am. Chem. Soc.* **2015**, *137* (9), 3197−3200.

(11) Kamat, P. V.; Tvrdy, K.; Baker, D. R.; Radich, J. G. Beyond Photovoltaics: Semiconductor Nanoarchitectures for Liquid-Junction Solar Cells. *Chem. Rev.* **2010**, *110* (11), 6664−6688.

(12) O'Regan, B.; Gratzel, M. A Low-Cost, High-Efficiency Solar Cell Based on Dye-Sensitized Colloidal TiO_2 Films. *Nature* **1991**, *353* (6346), 737−740.

(13) Li, W.; Wang, F.; Feng, S.; Wang, J.; Sun, Z.; Li, B.; Li, Y.; Yang, J.; Elzatahry, A. A.; Xia, Y.; Zhao, D. Sol−Gel Design Strategy for Ultradispersed TiO_2 Nanoparticles on Graphene for High-Performance Lithium Ion Batteries. *J. Am. Chem. Soc.* **2013**, *135* (49), 18300−18303.

(14) Shang, G.; Wu, J.; Huang, M.; Lan, Z.; Lin, J.; Liu, Q.; Zheng, M.; Huo, J.; Liu, L. Improving the Photovoltaic Performance of a Dye-Sensitized Solar Cell by Using a Hierarchical Titania Bur-like Microspheres Double Layered Photoanode. *J. Mater. Chem. A* **2013**, *1* (34), 9869−9874.

(15) Wang, H.; Wu, Y.; Xu, B.-Q. Preparation and Characterization of Nanosized Anatase TiO_2 Cuboids for Photocatalysis. *Appl. Catal., B* **2005**, *59* (3−4), 139−146.

(16) Chen, X.; Mao, S. S. Titanium Dioxide Nanomaterials: Synthesis, Properties, Modifications, and Applications. *Chem. Rev.* **2007**, *107* (7), 2891−2959.

(17) Sambur, J. B.; Novet, T.; Parkinson, B. A. Multiple Exciton Collection in a Sensitized Photovoltaic System. *Science* **2010**, *330* (6000), 63−66.

(18) He, J.; Benkö, G.; Korodi, F.; Polívka, T.; Lomoth, R.; Åkermark, B.; Sun, L.; Hagfeldt, A.; Sundström, V. Modified Phthalocyanines for Efficient Near-IR Sensitization of Nanostructured TiO_2 Electrode. *J. Am. Chem. Soc.* **2002**, *124* (17), 4922−4932.

(19) Zhang, H.; Cheng, K.; Hou, Y. M.; Fang, Z.; Pan, Z. X.; Wu, W. J.; Hua, J. L.; Zhong, X. H. Efficient CdSe Quantum Dot-Sensitized Solar Cells Prepared by a Postsynthesis Assembly Approach. *Chem. Commun.* **2012**, *48* (91), 11235−11237.

(20) He, J.; Zhang, S.; Sun, Z.; Cheng, W.; Liu, Q.; Jiang, Y.; Hu, F.; Pan, Z.; He, B.; Wu, Z.; Yan, W.; Wei, S. Realizing Hhigh Visible-Light-Induced Carriers Mobility in TiO_2-Based Photoanodes. *J. Power Sources* **2014**, *251* (0), 195−201.

(21) Dolbecq, A.; Dumas, E.; Mayer, C. R.; Mialane, P. Hybrid Organic−Inorganic Polyoxometalate Compounds: From Structural Diversity to Applications. *Chem. Rev.* **2010**, *110* (10), 6009−6048.

(22) Song, F.; Ding, Y.; Ma, B.; Wang, C.; Wang, Q.; Du, X.; Fu, S.; Song, J. $K_7[Co^{III}Co^{II}(H_2O)W_{11}O_{39}]$: a Molecular Mixed-Valence Keggin Polyoxometalate Catalyst of High Stability and Efficiency for Visible Light-Driven Water Oxidation. *Energy Environ. Sci.* **2013**, *6* (4), 1170−1184.

(23) Yin, P.; Wu, P.; Xiao, Z.; Li, D.; Bitterlich, E.; Zhang, J.; Cheng, P.; Vezenov, D. V.; Liu, T.; Wei, Y. A Double-Tailed Fluorescent Surfactant with a Hexavanadate Cluster as the Head Group. *Angew. Chem., Int. Ed.* **2011**, *50* (11), 2521−2525.

(24) Fu, N.; Lv, G. Graft of lacunary Wells-Dawson Heteropoly Blue on the Surface of TiO_2 and Its Photocatalytic Activity under Visible Light. *Chem. Commun.* **2009**, *24*, 3591−3593.

(25) Yin, J.; Qi, L.; Wang, H. Polyoxometalate-Assisted Synthesis of TiO_2 Nanoparticles and Their Applications in Aqueous Hybrid Electrochemical Capacitors. *ACS Appl. Mater. Interfaces* **2011**, *3* (11), 4315−4322.

(26) Du, D.-Y.; Qin, J.-S.; Li, S.-L.; Su, Z.-M.; Lan, Y.-Q. Recent Advances in Porous Polyoxometalate-Based Metal-Organic Framework Materials. *Chem. Soc. Rev.* **2014**, *43* (13), 4615−4632.

(27) Han, X.-B.; Zhang, Z.-M.; Zhang, T.; Li, Y.-G.; Lin, W.; You, W.; Su, Z.-M.; Wang, E.-B. Polyoxometalate-Based Cobalt−Phosphate Molecular Catalysts for Visible Light-Driven Water Oxidation. *J. Am. Chem. Soc.* **2014**, *136* (14), 5359−5366.

(28) Lu, M.; Xie, B.; Kang, J.; Chen, F.-C.; Yang; Peng, Z. Synthesis of Main-Chain Polyoxometalate-Containing Hybrid Polymers and Their Applications in Photovoltaic Cells. *Chem. Mater.* **2004**, *17* (2), 402−408.

(29) Sang, X.; Li, J.; Zhang, L.; Wang, Z.; Chen, W.; Zhu, Z.; Su, Z.; Wang, E. A Novel Carboxyethyltin Functionalized Sandwich-type Germanotungstate: Synthesis, Crystal Structure, Photosensitivity, and Application in Dye-Sensitized Solar Cells. *ACS Appl. Mater. Interfaces* **2014**, *6* (10), 7876−7884.

(30) Sang, X.-J.; Li, J.-S.; Zhang, L.-C.; Zhu, Z.-M.; Chen, W.-L.; Li, Y.-G.; Su, Z.-M.; Wang, E.-B. Two Carboxyethyltin Functionalized Polyoxometalates for Assembly on Carbon Nanotubes as Efficient Counter Electrode Materials in Dye-Sensitized Solar Cells. *Chem. Commun.* **2014**, *50* (93), 14678−14681.

(31) Li, J.-S.; Sang, X.-J.; Chen, W.-L.; Zhong, R.-L.; Lu, Y.; Zhang, L.-C.; Su, Z.-M.; Wang, E.-B. Photosensitive Polyoxometalate-Induced Formation of Thermotropic Liquid Crystal Nanomaterial and Its Photovoltaic Effect. *RSC Adv.* **2015**, *5* (11), 8194−8198.

(32) Weinstock, I. A. Homogeneous-Phase Electron-Transfer Reactions of Polyoxometalates. *Chem. Rev.* **1998**, *98* (1), 113−170.

(33) Wang, Y.; Li, H.; Wu, C.; Yang, Y.; Shi, L.; Wu, L. Chiral Heteropoly Blues and Controllable Switching of Achiral Polyoxometalate Clusters. *Angew. Chem., Int. Ed.* **2013**, *52* (17), 4577−4581.

DOI: 10.1021/acsami.5b03948
ACS Appl. Mater. Interfaces 2015, 7, 13714−13721

(34) Hiskia, A.; Mylonas, A.; Papaconstantinou, E. Comparison of the Photoredox Properties of Polyoxometallates and Semiconducting Particles. *Chem. Soc. Rev.* **2001**, *30* (1), 62−69.
(35) Izarova, N. V.; Pope, M. T.; Kortz, U. Noble Metals in Polyoxometalates. *Angew. Chem., Int. Ed.* **2012**, *51* (38), 9492−9510.
(36) Liu, C.-G.; Guan, W.; Yan, L.-K.; Su, Z.-M.; Song, P.; Wang, E.-B. Second-Order Nonlinear Optical Properties of Transition-Metal-Trisubstituted Polyoxometalate−Diphosphate Complexes: A Donor−Conjugated Bridge−Acceptor Paradigm for Totally Inorganic Nonlinear Optical Materials. *J. Phys. Chem. C* **2009**, *113* (45), 19672−19676.
(37) Wang, J.; Li, H.; Ma, N.-N.; Yan, L.-K.; Su, Z.-M. Theoretical Dtudies on Organoimido-Substituted Hexamolybdates Dyes for Dye-Sensitized Solar Cells (DSSC). *Dyes Pigm.* **2013**, *99* (2), 440−446.
(38) Wang, S.-M.; Liu, L.; Chen, W.-L.; Wang, E.-B.; Su, Z.-M. Polyoxometalate-Anatase TiO_2 Composites are Introduced into the Photoanode of Dye-Sensitized Solar Cells to Retard the Recombination and Increase the Electron Lifetime. *Dalton. Trans.* **2013**, *42* (8), 2691−2695.
(39) Li, L.; Yang, Y.; Fan, R.; Wang, X.; Zhang, Q.; Zhang, L.; Yang, B.; Cao, W.; Zhang, W.; Wang, Y.; Ma, L. Photocurrent Enhanced Dye-Sensitized Solar Cells Based on TiO_2 Loaded $K_6SiW_{11}O_{39}Co(ii)$-(H_2O)·xH_2O Photoanode Materials. *Dalton. Trans.* **2014**, *43* (4), 1577−1582.
(40) Wang, S. M.; Liu, L.; Chen, W. L.; Su, Z. M.; Wang, E. B.; Li, C. Polyoxometalate/TiO_2 Interfacial Layer with the Function of Accelerating Electron Transfer and Retarding Recombination for Dye-Sensitized Solar Cells. *Ind. Eng. Chem. Res.* **2014**, *53* (1), 150−156.
(41) Rocchiccioli-Deltcheff, C.; Fournier, M.; Franck, R.; Thouvenot, R. Vibrational Investigations of Polyoxometalates. 2. Evidence for Anion-Anion Interactions in Molybdenum (VI) and Tungsten (VI) Compounds Related to the Keggin Structure. *Inorg. Chem.* **1983**, *22* (2), 207−216.
(42) Nolan, A. L.; Burns, R. C.; Lawrance, G. A. Oxidation of $[Co^{II}W_{12}O_{40}]^{6-}$ to $[Co^{III}W_{12}O_{40}]^{5-}$ by Peroxomonosulfate in Strong and Weak Acid Solutions, an Example of Zero-Order Kinetics. *J. Chem. Soc., Dalton Trans.* **1998**, *18*, 3041−3047.
(43) Graham, C. R.; Finke, R. G. The Classic Wells-Dawson Polyoxometalate, $K_6[\alpha\text{-}P_2W_{18}O_{62}]\cdot 14H_2O$. Answering an 88 Year-Old Question: What Is Its Preferred, Optimum Synthesis. *Inorg. Chem.* **2008**, *47* (9), 3679−3686.
(44) Tong, X.; Wu, X. F.; Wu, Q. Y.; Zhu, W. M.; Cao, F. H.; Yan, W. F. Pentadecatungstotrivanadodiphosphoric Heteropoly Acid with Dawson Structure: Synthesis, Conductivity and Conductive Mechanism. *Dalton Trans.* **2012**, *41* (33), 9893−9896.
(45) Liu, J. F.; Ortéga, F.; Sethuraman, P.; Katsoulis, D. E.; Costello, C. E.; Pope, M. T. Trimetallo Derivatives of Lacunary 9-Tungstosilicate Heteropolyanions. Part 1. Synthesis and Characterization. *J. Chem. Soc., Dalton. Trans.* **1992**, *12*, 1901−1906.
(46) Bu, W. -F; Li, H.-L.; Sun, H.; Yin, S.-Y.; Wu, L.-X. Polyoxometalate-Based Vesicle and Its Honeycomb Architectures on Solid Surfaces. *J. Am. Chem. Soc.* **2005**, *127* (22), 8016−8017.
(47) Ito, S.; Chen, P.; Comte, P.; Nazeeruddin, M. K.; Liska, P.; Péchy, P.; Grätzel, M. Fabrication of Screen-Printing Pastes From TiO_2 Powders for Dye-Sensitised Solar Cells. *Prog. Photovoltaics* **2007**, *15* (7), 603−612.
(48) O'Regan, B.; Moser, J.; Anderson, M.; Grätzel, M. Vectorial Electron Injection into Transparent Semiconductor Membranes and Electric Field Effects on the Dynamics of Light-Induced Charge Separation. *J. Phys. Chem.* **1990**, *94* (24), 8720−8726.
(49) Zhai, Q. G.; Wu, X. Y.; Chen, S. M.; Zhao, Z. G.; Lu, C. Z. Construction of Ag/1,2,4-Triazole/Polyoxometalates Hybrid Family Varying from Diverse Supramolecular Assemblies to 3-D Rod-Packing Framework. *Inorg. Chem.* **2007**, *46* (12), 5046−5058.
(50) Lopez, X.; Carbo, J. J.; Bo, C.; Poblet, J. M. Structure, Properties and Reactivity of Polyoxometalates: A Theoretical Perspective. *Chem. Soc. Rev.* **2012**, *41* (22), 7537−7571.
(51) Liu, C. G.; Guan, W.; Song, P.; Su, Z. M.; Yao, C.; Wang, E. B. Second-Order Nonlinear Optical Properties of Trisubstituted Keggin and Wells-Dawson Polyoxometalates: Density Functional Theory Investigation of the Inorganic Donor-Conjugated Bridge-Acceptor Structure. *Inorg. Chem.* **2009**, *48* (17), 8115−8119.
(52) Jiang, T.; Xie, T.; Yang, W.; Chen, L.; Fan, H.; Wang, D. Photoelectrochemical and Photovoltaic Properties of p−n Cu_2O Homojunction Films and Their Photocatalytic Performance. *J. Phys. Chem. C* **2013**, *117* (9), 4619−4624.
(53) Lee, K. E.; Gomez, M. A.; Elouatik, S.; Demopoulos, G. P. Further Understanding of the Adsorption Mechanism of N719 Sensitizer on Anatase TiO_2 Films for DSSC Applications Using Vibrational Spectroscopy and Confocal Raman Imaging. *Langmuir* **2010**, *26* (12), 9575−9583.
(54) Ng, K. T.; Hercules, D. M. Studies of Nickel-Tungsten-Alumina Catalysts by X-ray Photoelectron Spectroscopy. *J. Phys. Chem.* **1976**, *80* (19), 2094−2102.
(55) Chen, X.; Dai, Y. C.; Zheng, Z. B.; Wang, K. Z. Photoelectrochemical Properties of Electrostatically Self-Assembled Multilayer Films Formed by a Cobalt Complex and Graphene Oxide. *J. Colloid Interface Sci.* **2013**, *402* (15), 107−113.
(56) Zhu, Q.; Qian, J.; Pan, H.; Tu, L.; Zhou, X. Synergistic Manipulation of Micro-Nanostructure and Composition: Anatase/Rutile Mixed-Shaped TiO_2 Hollow Micro-Nanospheres with Hierarchical Mesopores for Photovoltaic and Photocatalytic Applications. *Nanotechnology* **2011**, *22* (39), 395703.
(57) Wang, S.; Li, H. L.; Li, S.; Liu, F.; Wu, D. Q.; Feng, X. L.; Wu, L. X. Electrochemical-Reduction-Assisted Assembly of a Polyoxometalate/Graphene Nanocomposite and Its Enhanced Lithium-Storage Performance. *Chem.—Eur. J.* **2013**, *19* (33), 10895−10902.
(58) Bosch-Navarro, C.; Matt, B.; Izzet, G.; Romero-Nieto, C.; Dirian, K.; Raya, A.; Molina, S.-I.; Proust, A.; Guldi, D.-M.; Martí−Gastaldo, C.; Coronado, E. Charge Transfer Interactions in Self-Assembled Single Walled Carbon Nanotubes/Dawson-Wells Polyoxometalate Hybrids. *Chem. Sci.* **2014**, *5* (11), 4346−4354.
(59) Sun, Z. X.; Xu, L.; Guo, W. H.; Xu, B. B.; Liu, S. P.; Li, F. Y. Enhanced Photoelectrochemical Performance of Nanocomposite Film Fabricated by Self-Assembly of Titanium Dioxide and Polyoxometalates. *J. Phys. Chem. C* **2010**, *114* (11), 5211−5216.
(60) Bisquert, J.; Zaban, A.; Greenshtein, M.; Mora-Seró, I. Determination of Rate Constants for Charge Transfer and the Distribution of Semiconductor and Electrolyte Electronic Energy Levels in Dye-Sensitized Solar Cells by Open-Circuit Photovoltage Decay Method. *J. Am. Chem. Soc.* **2004**, *126* (41), 13550−13559.
(61) Wang, Q.; Moser, J.-E.; Grätzel, M. Electrochemical Impedance Spectroscopic Analysis of Dye-Sensitized Solar Cells. *J. Phys. Chem. B* **2005**, *109* (31), 14945−14953.

DOI: 10.1021/acsami.5b03948
ACS Appl. Mater. Interfaces 2015, 7, 13714−13721